The Impact of Absorption on SERS Detection

Thesis

Presented in Partial Fulfillment of the Requirements for the Degree Master of Science in the Graduate School of The Ohio State University

By

Lindsey Ann Speare, B.S.

Graduate Program in Chemistry

The Ohio State University

2024

Thesis Committee:

Zac Schultz, Advisor

Heather Allen

Abraham Badu-Tawiah

Abstract

Surface enhanced Raman spectroscopy (SERS) is a highly sensitive chemically specific method that is capable of trace analyte detection.[1–3] One challenge with SERS is that the spectrum must be stable and consistent to accurately identify compounds. The localized surface plasmon resonance (LSPR) that enhances the Raman signal can cause chemical transformations on molecules near the nanoparticles. The SERS peaks can fluctuate in intensity and position, indicating the presence of transient species like ions or other products from photo-induced reactions. The background of SERS spectra has also been observed to increase or decrease depending on the experiment.[4–9] All of these effects are convoluted with the role of heating that also results from excitation of the LSPR. This thesis attempts to identify spectral fluctuations due to heating as well as to shed some light on the inner workings of the background observed in the spectra.

Dedication

I dedicate this thesis to my parents, partner, and beloved friend, Riana Morrison.

Acknowledgements

This work is supported by award CHE- from the National Science Foundation.

I would like to thank my advisor, Zac Schultz, for being so supportive and direct throughout my research. He was always available to meet despite his countless other duties as Vice Chair of Graduate Studies as well as tending to other lab members. He voiced his support and always gave words of encouragement when he knew I was in distress. His belief in me helped me get through challenging times during this thesis and I am grateful to have picked such a wonderful advisor.

I would also like to thank my amazing lab members for their advice and help with instruments as well as their constant attendance at practice exams despite their busy schedules. I also could not have done it without friends who I have met through Ohio State as their support and friendship has provided significant comfort through this experience.

Finally, I would like to thank my family, my partner, and my dog for being my peace during a very dynamic time in my life. I'm so grateful to have such a wonderful support system that has cheered me on since the beginning as I could not have done it on my own.

Vita

- College Credit Plus at Kent State (Fall 2017)
- Graduated from Stow-Munroe Falls High School (2018)
- Research for Undergraduate Experience at Kent State University (2019)
- Employed under Torsten Hegmann at Kent State University (2021)
- Ohio Space Grant Consortium scholarship (2021-2022)
- Graduated Kent State University with BS in chemistry and a minor in physics (2022)
- Graduate Teaching Associate, Chemistry, The Ohio State University (2022-present)

Publications

Fields of Study

Major Field: Chemistry

Table of Contents

Abstract i

Dedication ii

Acknowledgements iii

Vita iv

List of Figures vi

Chapter 1: Introduction 1

1.1 Motivation 1

1.2 Raman Spectroscopy 1

1.3 Surface Enhanced Raman Spectroscopy 5

Chapter 2: Methods 17

2.1 AuNP Synthesis & Functionalization 17

2.2 AgPAN Fiber Synthesis 17

2.3 Characterization 18

2.4 Raman Spectroscopy 19

2.5 Measuring the Laser Spot 20

2.6 Absorption Experiment 21

Chapter 3: Results & Discussion 22

3.1 Power Study 22

3.2 Heating Via Absorption 24

3.3 The Background Trend 30

Chapter 4: Conclusion 38

Bibliography 40

List of Figures

Figure 1. Jablonski diagram with the Stokes, Rayleigh, and anti-Stokes processes..... 2

Figure 2. Representation of a plasmon resonance.[14] 5

Figure 3. The extinction spectrum of gold nanospheres increasing in diameter.[20] 6

Figure 4. The longitudinal peak shift of nanobars and nanorice in response to aspect ratio.[18] 7

Figure 5. The rapid decay of enhancement within a nanoparticle gap.[23] 9

Figure 6. The two methods of charge transfer.[30] 10

Figure 7. SERS spectrums of 4-cyanothiolphenol on gold nanoparticles in air and solution before with increasing illumination powers.[33] 12

Figure 8. A log histogram of the average anti-Stokes to Stokes ratio of each SERS intensity fluctuation in the range of ~300 to ~2200 cm^{-1}.[37] 13

Figure 9. The average spectrums and mesh plots of MBA with increasing laser power densities.[9] 15

Figure 10. Cation and anion assignments to spectral fluctuations seen during irradiation.[9] 16

Figure 11. The extinction spectrum of MBA functionalized nanoparticles 18

Figure 12. Measuring the laser spot for the 633 nm laser using the 50x objective 20

Figure 13. Schematic of laser and LED illuminating the sample in tandem 21

Figure 14. Raman spectra of MBA functionalized gold nanoparticles using high and low laser power..... 22

Figure 15. Laser power study of MBA functionalized gold nanoparticles using the 633 nm laser 23

Figure 16. The extinction spectrum of MBA functionalized gold nanoparticles with the 633 nm laser and LEDs indicated 24

Figure 17. The average signal for increasing 455 nm LED powers for dry and aqueous MBA functionalized gold nanoparticle samples using the 633 nm laser 25
Figure 18. The average signal for increasing 505 nm LED powers for dry and aqueous MBA functionalized gold nanoparticle samples using the 633 nm laser 27
Figure 19. Schematic of the old LED replacing the white light and the new LED 29
Figure 20. The average signal for increasing 450 nm LED powers for dried MBA functionalized gold nanoparticles with a plot of the background intensity at the respective power density. Then the average signal for increasing 505 nm LED powers for silver nanoparticles encapsulated in PAN fibers with a plot of the background intensity at the respective power density 30
Figure 21. The average signal for increasing 550 nm LED and 635 nm powers for dried MBA functionalized gold nanoparticles using the 785 nm laser and plots with peak area and background intensity at the respective LED power 32
Figure 22. The background increasing due to increasing laser power on gold nanodisks and on MBA functionalized gold nanoparticles.[6] 33
Figure 23. The LSPR of the MBA functionalized nanoparticles with lines indicating the position of the LEDs and lasers 35
Figure 24. The normalized average spectrum of the highest LED power for each LED used with the 633 nm laser 36

Chapter 1: Introduction

1.1 Motivation

Surface enhanced Raman spectroscopy (SERS) is a highly sensitive chemically specific method that is capable of trace analyte detection.[1–3] One challenge with SERS is that the spectrum must be stable and consistent to accurately identify compounds. The localized surface plasmon resonance (LSPR) that enhances the Raman signal can cause chemical transformations on molecules near the nanoparticles. The SERS peaks can fluctuate in intensity and position, indicating the presence of transient species like ions or other products from photo-induced reactions. The background of SERS spectra has also been observed to increase or decrease depending on the experiment.[4–9] All of these effects are convoluted with the role of heating that also results from excitation of the LSPR. This thesis attempts to identify spectral fluctuations due to heating as well as to shed some light on the inner workings of the background observed in the spectra.

1.2 Raman Spectroscopy

Raman spectroscopy is a popular method for many researchers due to its ability to easily and non-destructively probe vibrational modes that are specific to molecules. This technique can analyze solids, liquids, and gases and can be easily integrated into most experiments. Its versatility enables a quick and straightforward sample preparation. Analytes can also be detected[1–3] and even

quantified when the signals are enhanced.[10–12] These traits represent only a fraction of Raman's inherent advantages.

When a molecule is irradiated, absorption and scattering of the light will occur. Absorption involves the promotion of an electron from a lower to higher energy state while photons are scattered due to the interaction between the incident light and the molecule. Scattering is typically elastic, meaning that the emission is equal to the incident energy, which is termed Rayleigh scattering. Inelastic scattering is significantly less common as it only occurs once out of every million scattered photons.[13] The energy of the scattered photons can be higher (anti-Stokes scattering) or lower (Stokes scattering) than the incident light.

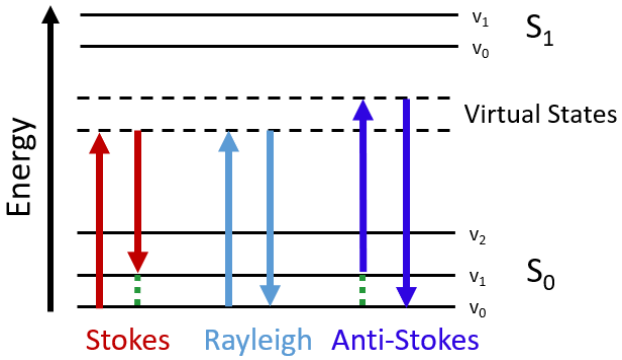

Figure 1. Jablonski diagram with the Stokes, Rayleigh, and anti-Stokes processes.

In **Figure 1**, a Jablonski diagram is shown with the solid lines as vibrational states within a specific electronic energy level and the dotted lines as virtual states. Excited states are best

described as a probability distribution, with the maximum defined as the excited state. The virtual states are then low probability instance of the respective excited state and contains the same energy. The arrows pointing up represent the excitation pathway while the ones pointing down represent the relaxation pathway. The green dashed lines represent the change in energy between these two processes, which are indicative of specific vibrational modes within the molecules of interest. Often these phenomena are reported as Raman shifts, which are commonly reported in wavenumbers (cm^{-1}). Therefore, a decrease in the scattered photon energy corresponds to Stokes scattering, while an increase indicates anti-Stokes scattering. As a result, Rayleigh scattering is observed at 0 cm^{-1} since it is elastically scattered and represents the same energy as the excitation source. Usually, the Stokes region is used for analysis due to the higher population of electrons in the ground state at room temperature rather than a vibrationally excited state, which is needed for anti-Stokes scattering. This is explained by **Equation 1** where I_{AS} is the intensity of the anti-Stokes peak for a given mode and I_S is the intensity of the Stokes peak for the same mode, h is Planck's constant, ν is the frequency, k_B is Boltzmann's constant, and T is the temperature.

$$\frac{I_{AS}}{I_S} \propto e^{-h\nu/k_BT} \qquad \text{(Eq. 1)}$$

The best modes to pick are well defined and intense in both regions while also sensitive to temperature changes.[14] It is vital that the respective anti-Stokes peak has a quantifiable intensity, otherwise the calculation will be unreliable. Low energy shifts are ideal since the populations of the exited states will be more occupied than at higher energy shifts.

Unfortunately, not all vibrational modes are Raman active because Raman modes are dependent on a change in polarizability. Infrared (IR) spectroscopy is another vibrational spectroscopic method that measures absorption, but the analyte must have a change in dipole

moment to have IR active modes. These modes can be active in both Raman and IR, or exclusively Raman or IR active within a molecule, illustrating why IR is complementary to Raman.[13]

A major advantage of Raman over IR is that Raman can use lasers in the visible light region since it measures scattering rather than absorption. Raman often uses a lower wavelength in the visible regime, therefore it has better spatial resolution than IR. This is shown in **Equation 2**, where x is the minimum resolvable distance, λ is the incident wavelength, d is the distance between the sample and the objective, and D is the illuminated diameter of the lens.

$$x = \frac{1.22\lambda d}{D} \qquad \text{(Eq. 2)}$$

Utilizing visible light also allows aqueous solutions to be analyzed because water does not absorb strongly in the visible region but does in the IR region, causing a broad background.

The primary disadvantage of Raman, as previously mentioned, is the low frequency of inelastic scattering, which ultimately causes the Raman signals to be weak. Since IR spectroscopy measures absorbance, a more likely event, the signal is much more intense. The intensity of the Raman signal, I, is given by **Equation 3** where K contains constants like the speed of light, l is the laser power, α is the polarizability of the molecule, and ω is the frequency of the incident light.[13]

$$I = Kl\alpha^2\omega^4 \qquad \text{(Eq. 3)}$$

Increasing the laser power will increase the signal, but too much power can begin to damage or burn the analyte due to local heating. Hence, it is important to conduct a laser power study to determine the optimum irradiation to use for excitation, especially when studying the effects of heating. However, even with high laser powers, some Raman modes can be unquantifiable above the noise due to the inherently infrequent inelastic photon scattering. Fortunately, these signals can

be enhanced by incorporating metallic structures near the analyte in a technique known as Surface Enhanced Raman Spectroscopy (SERS).

1.3 Surface Enhanced Raman Spectroscopy

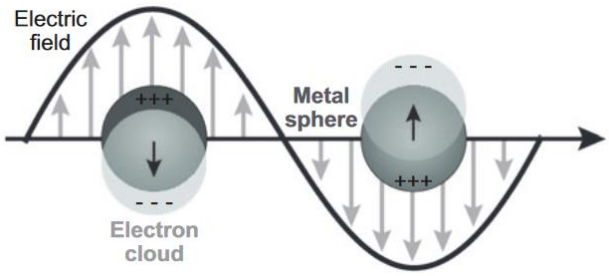

Figure 2. Representation of a plasmon resonance.[15]

SERS has the potential to enhance Raman signals to the range of 10^6 and beyond.[15] It utilizes metals like gold, silver, and copper to provide enhancement. Typically, gold and silver are used due to their high electron density and because they both have a negative real part and a near-zero imaginary part of their respective dielectric constants.[16–18] The dielectric constant describes how easily the material can be polarized in an electric field and is dependent on the incident frequency. The real part pertains to scattering while the imaginary to absorption.[13] Bulk metals are not considered dielectric materials due to their high conductivity. However, when noble metals have their surface roughened or are synthesized into nanoparticles, they have a high density of electrons that warrants a dielectric constant in the visible or IR region. This enables the potential

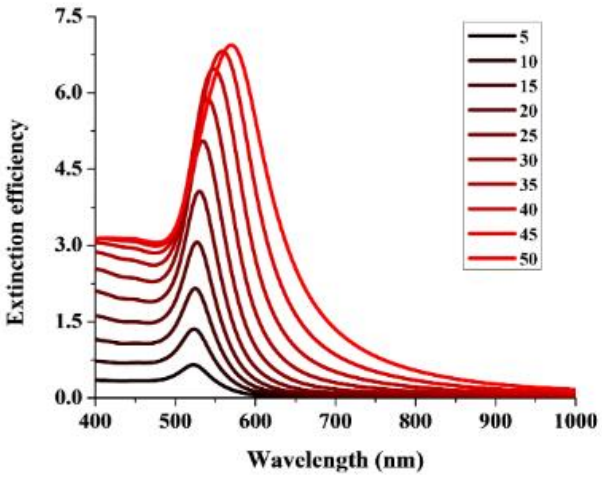

Figure 3. The extinction spectrum of gold nanospheres increasing in diameter from 5 to 50 nm.[21]

formation of a plasmon.[18] When incident light irradiates these particles, their free electrons oscillate in the opposite direction of the wavelength, which induces a localized surface plasmon resonance (LSPR, **Figure 2**) that generates a large electric field at the surface, enhancing Raman scattering. This plasmon has a resonant frequency where it absorbs and scatters light the most. This extinction maximum can be measured using a UV-vis spectrometer. The LSPR shifts as a result of the dielectric constant which is dependent on the size and morphology of the nanoparticle.[19,20] Increasing the surface area or number of edges to a nanoparticle will shift the LSPR to a longer wavelength (red shift).[19,21,22] In **Figure 3**, the LSPR of gold nanospheres with increasing radius (5 to 50 nm) depicts this shift. When spheres are irradiated, there is no directional dependence on the particle since the diameter of the sphere is consistent. However, when a particle that has an aspect ratio larger than 1 is irradiated, one axis is longer than the other, which excites two plasmons resonances, leading to two LSPR peaks. The peak corresponding to the short axis is

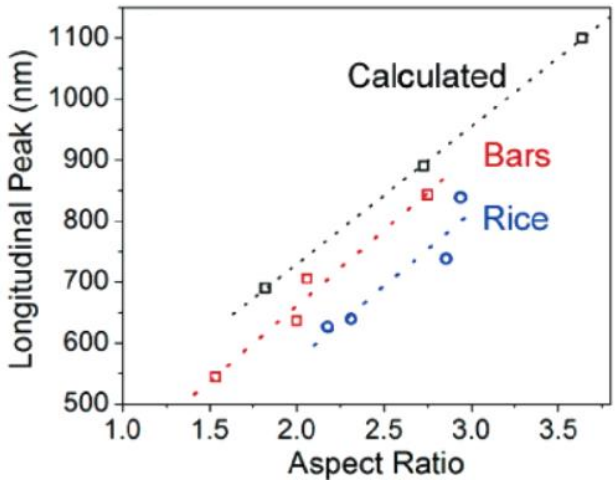

Figure 4. The longitudinal peak shift of nanobars (red) and nanorice (blue) in response to aspect ratio. The calculated shift of ideal nanobars is in black.[19]

the transversal mode and it will appear at a lower wavelength resonance than the longitudinal mode, which corresponds to the long axis. Nanorods can have various aspect ratios, so they possess two tunable plasmon resonances. In **Figure 4**, the longitudinal LSPR shifts of nanobars and nanorice were investigated to determine their dependence on aspect ratio since the transverse mode maintained a relatively constant energy.[19] The nanorice had soft edges compared to the bars which were more pronounced, causing the bars to have a larger red shift. Both nanostructures were seen to shift linearly with increasing aspect ratio, as expected. The experimental nanobars had less of a red shift when compared to the calculated shift. This is explained by the experimental bars not having perfect corners like the calculation.[19,23] The ability to tune the LSPR is a major advantage as it can be tailored near the excitation source.

The magnitude of the surface-enhanced Raman signal relative to the spontaneous Raman signal is termed the enhancement factor (EF). The EF of a single nanoparticle is approximated to

be the field enhancement at the nanoparticle to the fourth power. The power of four comes from the enhanced incident electric field localized to the nanoparticle as well as the reradiation of the scattering from molecules near the surface. As previously mentioned, in practice, the EF can be magnitudes larger and can be determined using **Equation 4** where I_{SERS} is the surface enhanced Raman signal, N_{surf} is the number of molecules bound to the metal structures, I_{NRS} is the normal Raman intensity, and N_{vol} is the number of molecules in the sample.[15]

$$EF = \frac{(I_{SERS}/N_{surf})}{(I_{NRS}/N_{vol})} \quad \text{(Eq. 4)}$$

There are two effects that are known to generate to this enhancement, however, their relative contributions are not clear. The first phenomenon is known as the electromagnetic (EM) enhancement. This phenomenon attributes the Raman enhancement to the molecule being very close or adsorbed onto the surface of the nanoparticle where the electric field is localized. When two particles are within a few nanometers of each other, their plasmons couple causing their electric fields to constructively interfere.[16] The largest enhancement occurs in the center of the gap, as depicted in **Figure 5**, and these regions are referred to as hot spots.[24] Hot spots can also generate at corners and edges on the nanoparticle[25,26] or in gaps within one.[27,28] The nanoparticles need to be within ~1 to 10 nm of each other to couple, but the greatest enhancement occurs when they are within one nanometer.[17] The enhancement decreases when the separation is less than 1 nm, which is thought to be a result of quantum tunneling.[29] Close proximity of the analyte to the particle allows electrons within the analyte to interact with the plasmon, especially when it is within a hot

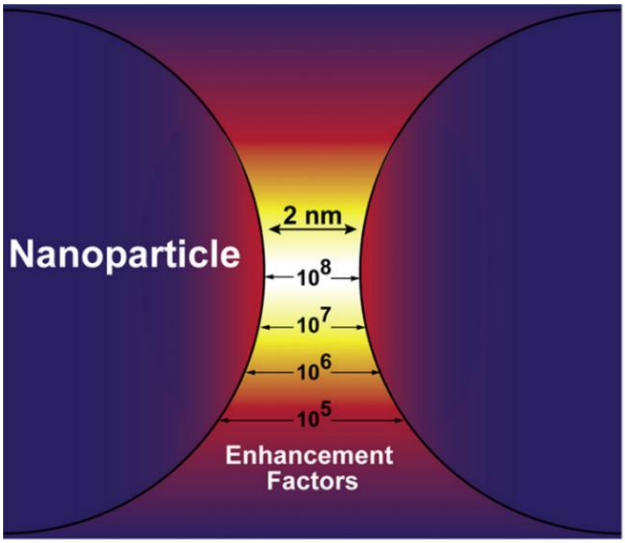

Figure 5. Illustration of the rapid decay of enhancement within a nanoparticle gap.[24]

spot.[13] **Equation 5** describes the relationship between Raman mode intensity (I_{SERS}) and the distance between the nanoparticle surface and the analyte (r), where a is the radius of the particle.[15]

$$I_{SERS} = \left(\frac{a+r}{a}\right)^{-10} \quad \text{(Eq. 5)}$$

Equation 5 explains why the signal intensity decreases rapidly as the molecule moves away from the surface. This distance dependence was studied using pyridine as the analyte and silver nanoparticles with varying layers of aluminum oxide as the substrate. Placing the analyte on the nanoparticle surface generated the greatest signal while a 1.6 nm layer of aluminum oxide caused the signal to decrease by ~75%.[30]

The second theory, chemical enhancement, relies on chemical changes to the molecule at the metallic surface. In one instance, it is speculated that the bond creates a surface species containing the analyte and some metal atoms, allowing the transfer of electrons and holes.

Enhancement is thought to come from the new electronic states produced from bond formation. Due to the constraint that molecules must be bound, the enhancement should increase only in the adsorbed monolayer since beyond that would be too far to be detected.[13] In a second instance, when the LSPR decays, the energy is absorbed by the nanostructure, producing energetic electrons (hot electrons or carriers) and leaving behind energetic vacancies known as hot holes. These hot electrons can decay further to give a high concentration of low energy carriers, which are at or above the energy level of the lowest unoccupied adsorbate states.[31]

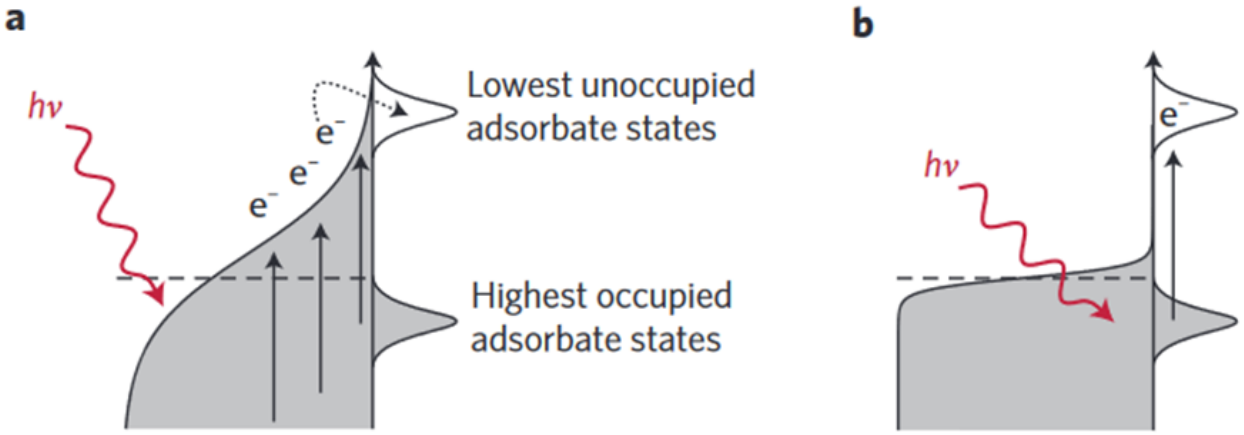

Figure 6. The two methods of charge transfer: indirect (a) and direct (b) where hv represents the incident light and the dotted line represents the Fermi energy of the nanoparticle.[31]

This excites the electron, allowing it to participate in chemical reactions, named indirect charge transfer (**Figure 6a**). Hot carriers can also move directly from the metal's highest occupied state into the molecule's lowest unoccupied state, which is known as direct charge transfer (**Figure 6b**).

The result of either mechanism produces products or transient species like radicals and ions, which appear as intensity or peak position fluctuations in the Raman spectrum.[31] These changes in chemistry can enhance Raman signals. Overall, it appears that both electromagnetic and chemical enhancement seem to contribute.[13]

When SERS was discovered, roughened metal surfaces were used as substates and gave an EF of ~10^6. It was believed that the EM enhancement contributed 10^4 while only 10^2 came from chemical enhancement.[15] Recently, nanoparticles of various morphologies are utilized and have enhancement factors ranging from 10^5 to 10^{13}.[15,25,28,32,33] It is conceivable that chemical enhancement may contribute more than what is currently assumed, which will be considered during this investigation.

As previously mentioned, high laser power will cause local heating, potentially damaging or burning the sample. In **Figure 7**, Zeng et al. studied 4-cyanothiolphenol on gold nanosphere (80 nm) aggregates in air and water to determine their response to temperature.[34] They found that the signal decreased significantly in air due to its low thermal conductivity. It is hypothesized that the decreased signal is from nanoparticles melting,[35] destroying the hot spots, or from analyte desorption.[34]

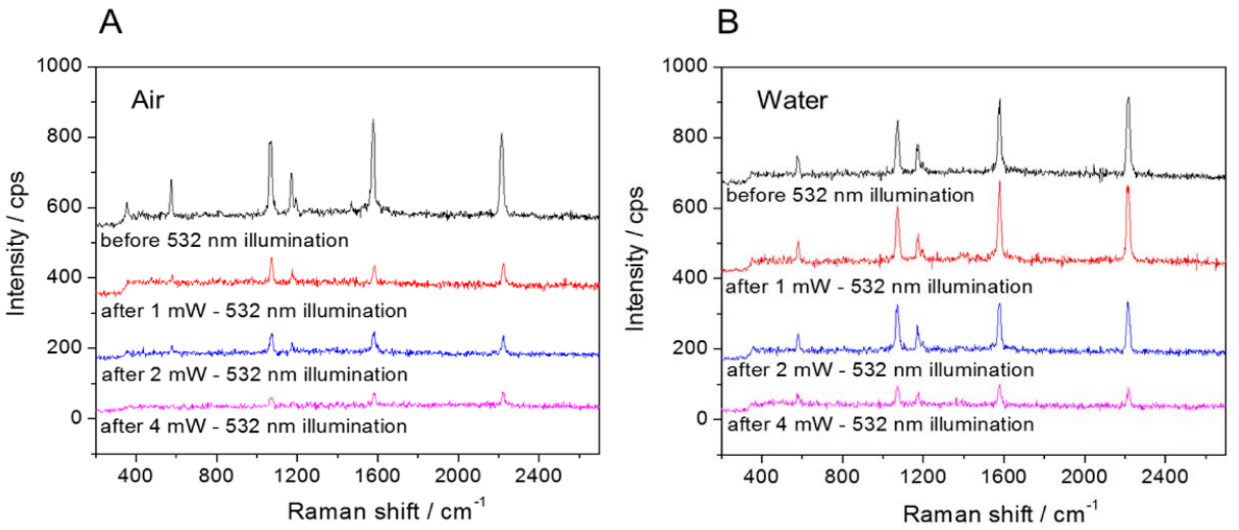

Figure 7. SERS spectrums of 4-cyanothiolphenol on gold nanoparticles in air (a) and solution (b) before illumination and with increasing illumination powers.[34]

Xu et al. saw the intensity decrease as well as red shifting due to local heating.[36] They investigated the effects of heating using a silicon platform with gold nanorods standing upright in an ordered array. This substrate was heated using a ceramic chip that was large enough to also heat the control sample, a silicon platform. They analyzed the SERS spectra from 293 to 424 K. As the temperature increased, the silicon peak red shifted but also decreased in intensity for both samples. The red shifting is theorized to be from temperature dependent volume expansion of silicon. The SERS substrate also had a larger response than the bare silicon due to its temperature sensitivity increasing.[36] However, Saikin et al. suggests that these shifts are influenced by the adsorbate's vibrational modes. They saw modes that included the metal and analyte were blue shifted (like a sulfur – gold bond), while modes originating from the molecule were shifted to lower energy.[37]

As previously mentioned, the excitation of the LSPR can cause hot carriers to form, which can in turn produce products or transient species that affect the spectra. Schmidt et al. studied SERS intensity fluctuations (SIFs) of benzenethiol dried on a silver film over silica nanoparticles.[38] They discovered that these events occur with equal probability over the Stokes and anti-Stokes region. As they increased the laser power from ~0.5 mW to ~1 mW it created SIFs with a larger anti-Stokes to Stokes ratio (**Equation 1**).[38]

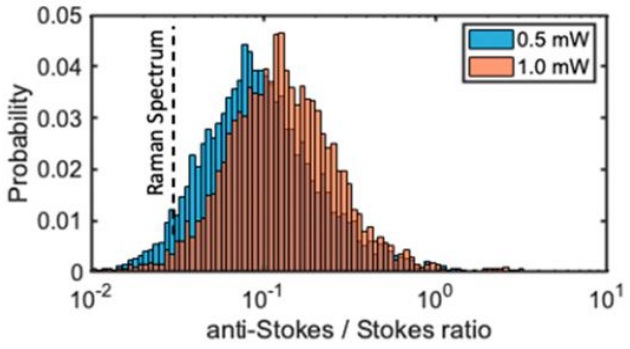

Figure 8. A log histogram of the average anti-Stokes to Stokes ratio of each SERS intensity fluctuation in the range of ~300 to ~2200 cm^{-1}. The ratio of neat benzenethiol using Raman (0.027) is represented by the dotted line.[38]

Typically, the ratio will remain below 1. However, Schmidt et al. found that SIFs in the anti-Stokes region can amplify the region for short periods of time which results in a ratio greater than 1.[38] This is shown in **Figure 8**, where the ratio of SIF events in the range of ~300 to ~2200 cm^{-1} are plotted as a logarithmic histogram. Approximately 0.9% of events at 1.0 mW have a ratio

above 1, which would estimate an unreasonably high temperature. They suspect this increase is due to the hotspot preferring to enhance certain portions of the spectra as well as the construction and destruction of hot spots. This reconstruction of the nanoparticle surface does not degrade the sample, as carbon contamination would appear in the spectra (strong, broad peak at ~1300 cm^{-1}). These SIFs were seen to last anywhere from 10 μs to 10 ms. It is theorized these high-speed fluctuations could originate from the analyte rotating on the substrate since it is unlikely that they would move laterally.[38]

Zoltowski et al. utilized wide field imaging and point scanning SERS to compare spectral fluctuations from single particles and agglomerates as well as signal stability from a silica shell[9]. Wide field spectral imaging disperses the response from the nanoparticles into its zeroth and first order diffraction. The zeroth order provides a spatial image while the first order gives the spectral response. They used 4-mercaptobenzoic acid (MBA) on gold nanospheres with and without a silica shell as their analyte and substrate.

When single particles were analyzed using wide field imaging, they found that frequency fluctuations occurred at a much lower laser power density (31 kW/cm^2) than when using point spectroscopy (194 kW/cm^2). They suspect that aggregates are being irradiated during point spectroscopy, which allows hot carriers to transfer between nanoparticles rather than to the analyte. In **Figure 9**, isolated nanoparticles are irradiated at increasing laser powers, displaying spectral fluctuations. One thousand 100 ms acquisitions were taken and the average is shown in 9a. In 9b, mesh plots of these acquisitions are presented, clearly showing spectral events. At low powers (0.93 kW/cm^2) only intensity fluctuations occurred; however, as the power increased (31.42 kW/cm^2), more frequency fluctuations were observed. Nanoparticles with a silica shell required a higher power to induce SIFs due to the added stability originating from the silica.[9]

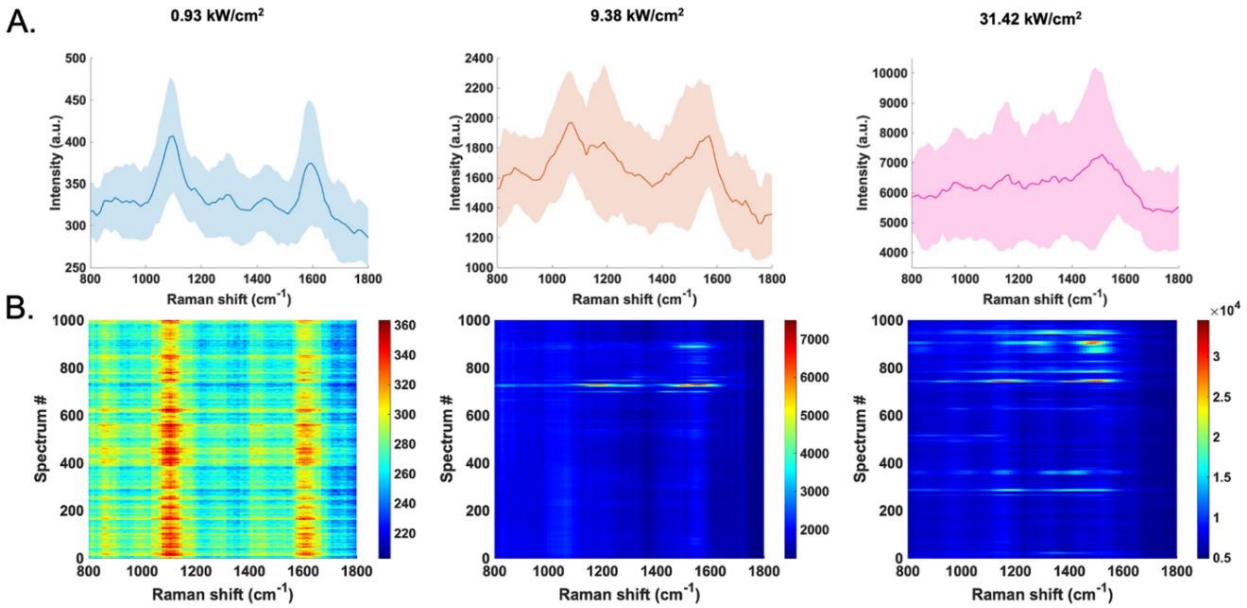

Figure 9. The average spectrums of MBA with increasing laser power densities (a) and their respective mesh plots (b) using wide field imaging.[9]

To elucidate the origin of these fluctuations, point spectroscopy was used to identify their peak positions because wide field has reduced spectral resolution. From previous DFT calculations of MBA's radical cation and anion, they were able to identify some peaks from both species (**Figure 10**).[9] This indicates that hot carriers can induce chemical changes in the analyte.

During this experiment, they noticed that as the power increased so did the background of the spectra. For the nanoparticles without a shell, it increased until the highest power where it decreased slightly, while the nanoparticles with a shell exhibited a linear increase.[9] It has been thought that the background originates from the metal;[5] however, the exact mechanism that this trend originates from is not fully understood. Mahajan et al. suggests that electron withdrawing groups pull electrons to the metal surface, reducing the dielectric screening, which increases the

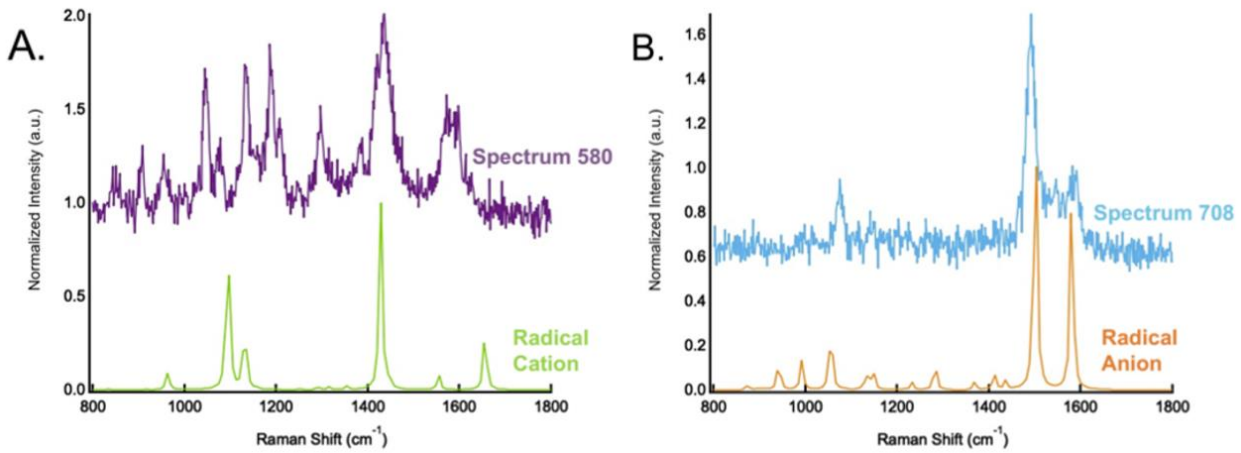

Figure 10. Cation (a) and anion (b) assignments to spectral fluctuations seen during irradiation.[9]

background.[5] Another group reports that this effect comes from inelastic scattering within the metal, increasing the conductivity of gold.[4] In this thesis, I investigate the background effect and the possible origin of spectral fluctuations.

Chapter 2: Methods

2.1 AuNP Synthesis & Functionalization

To synthesize gold nanoparticles, chloroauric(III) acid ($HAuCl_4 \cdot 3H_2O$) and sodium citrate ($Na_3C_6H_5O_7 \cdot 2H_2O$) were purchased from Sigma-Aldrich. A synthesis previously reported[39] was followed with adjustments. 50 mL of chloroauric acid (0.25 mM) was heated (350°C) until it began to boil. Then 625 μL of 1% trisodium citrate was added. The heat was immediately turned off and it was allowed to cool to room temperature.

To functionalize these nanoparticles, 4-mercaptobenzoic acid (MBA) was purchased from Sigma-Aldrich. The gold nanoparticle solution (~69 nm) was added into several centrifuge tubes (1 mL) and centrifuged at 6,000 rpm for 20 minutes. The citrate was removed and distilled water was added along with 1 μL of MBA (40 mM). They were shaken for 40 minutes then centrifuged at 6,000 rpm for 20 minutes. The supernatant was removed then the particles were resuspended in 500 μL of distilled water.

2.2 AgPAN Fiber Synthesis

Polyacrylonitrile (PAN, Mw 150,000) was purchased from Sigma-Aldrich, dimethylformamide (DMF) was purchased from Fischer Scientific, and dried silver nanoparticles (50 nm) were purchased from Sky Springs Nanomaterials, Inc. To synthesize the nanoparticle-polymer solution, 4.0 mg of silver nanoparticles and 3.6 g of DMF were added to a vial and then it was sonicated for thirty minutes. 0.4 g of PAN was added to the vial along with a stir bar, which

stirred overnight. Then the solution was added to a syringe, which was placed in a syringe pump (Havard Apparatus Pump II Elite). The electrospinning configuration was in a nitrogen atmosphere to keep the humidity below 20%. The tip of the syringe was 15 cm away from the collection plate, which had aluminum foil covering it. A square indium-tin-oxide (ITO) glass slide (Sigma-Aldrich) was taped to the plate to collect the fibers. The power supply used was a Spellman CZE 1000R to provide a positive voltage to the needle tip as well as to ground the ITO slide. The voltage was set to 10 kV then the solution spun at 1 mL/hr for 8 minutes. This was conducted in Dr. Olesik's lab with their equipment, reagents, and assistance.

2.3 Characterization

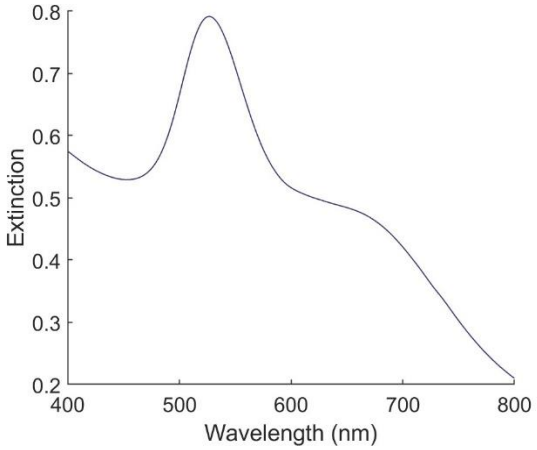

Figure 11. Extinction spectrum of MBA functionalized nanoparticles.

A Malvern Nanosight NS 300 equipped with a green laser was used to determine the diameter of the nanoparticles. The analysis used a camera level of 7 and a detection level of 3. The extinction spectrum was obtained using an Aligent Cary 4000 UV-Vis spectrophotometer in the range of 200-800 nm with 0.01 nm resolution at 600 nm/min. The ensemble extinction spectrum of the MBA functionalized gold nanoparticles is shown in **Figure 11**. The maximum peak at 528 nm is indicative of single particles while the broad shoulder at ~660 nm implies the presence of aggregates.

2.4 Raman Spectroscopy

Raman measurements were made on a Leica DM LM attached to a Renishaw inVia using a 632.8 nm HeNe laser (Thorlabs). The laser was focused onto the sample using a 50X objective (NA = 0.75) for dry samples and an immersive 63X objective (NA = 0.9) for solution-based samples. Raman scattering was collected through the same objective and directed to the spectrometer.

Raman measurements were also made on a custom Raman microscope equipped with a 784.55 nm diode laser (Oxxius). The laser was focused through a 50X objective (NA = 0.75). The scattering was collected through the same objective by an Isoplane SCT320 spectrograph harnessed with ProEM: 1600^2 eXcelon 3 CCD detector (Princeton Instruments).

2.5 Measuring the Laser Spot

The laser spot size for each instrument was determined by monitoring the change in intensity from the 520 cm^{-1} Si band using a gold/silicon interface. The laser was focused onto the silicon region near the border then 1s acquisitions were taken at each position as it moved onto the gold. The regions of pure silicon were fit with a line as well as the region of gold. The difference between these regions allowed the 90-10% Si intensity region to be determined. In **Figure 12**, this range is marked by the yellow lines. This indicates a laser spot size of 1.36 µm in diameter using the 50X objective with the 633 nm laser on the Renishaw inVia. Doing the same with the 63X immersive objective yielded a spot size of 1.12 µm with the 633 nm laser. For the custom microscope, the spot size was determined to be 6.67 µm for the 50X objective, when using the 785 nm laser.

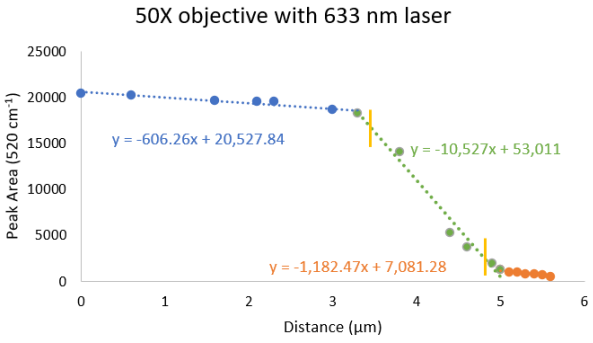

Figure 12. Measuring the laser spot with a silicon and gold boundary. The silicon (blue) and gold (orange) regions are shown with the difference between them in green. The 90-10% region is marked by the yellow lines.

2.6 Absorption Experiment

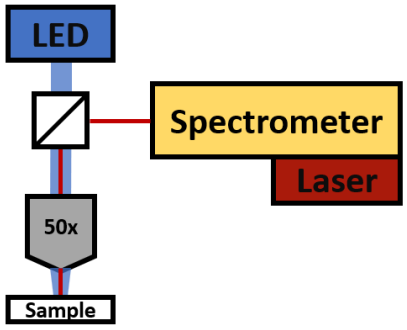

Figure 13. Schematic of laser and LED illuminating the sample in tandem.

For the heating experiment, the desired LED was mounted on the top illumination mount of the microscope. 455 nm (Thorlabs), 505 nm (Thorlabs), and a multichannel LED (450 nm, Cool LED pE-400 max) were each used in tandem to the laser as shown in **Figure 13**. The LEDs and laser lines were not visible in the Stokes spectra since a 633 nm long pass filter was employed before the signal reaches the detector in the Renishaw and a 785 nm notch filter was used in the custom microscope. The first scan was taken without the LED then the LED was turned on and acquisitions were taken at each power. After the highest power, the LED was turned off and another scan was taken to ensure no damage occurred. On the Renishaw inVia and the custom microscope, 100 spectra were acquired with 1s acquisition time per scan. The main difference between the microscopes is that the Renishaw can analyze a 575 cm^{-1} range using 1s acquisitions while the custom microscope can analyze a 1600 cm^{-1} range using 1s acquisitions. The range utilized always

included the intrinsic 1586 cm^{-1} peak for MBA or the 2242 cm^{-1} peak for PAN. The power density for the LED is an estimate as the illuminated area was not measured.

Chapter 3: Results & Discussion

3.1 Power Study

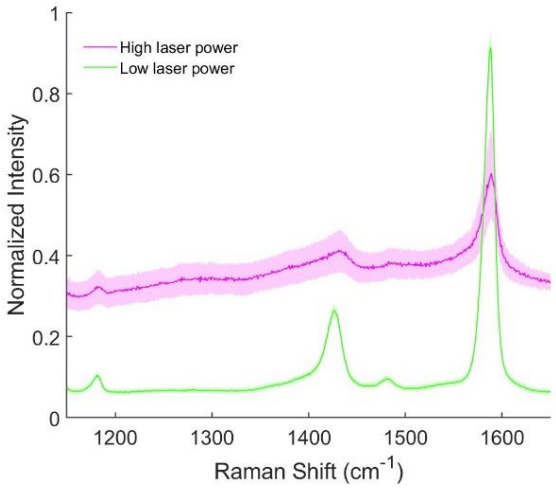

Figure 14. Raman spectra of MBA functionalized gold nanoparticles using 261.57 kW/cm² (dark purple) and 5.85 kW/cm² (green) using the 633 nm laser. The standard deviations are the shaded regions.

As previously mentioned, it is best to conduct a laser power study for each type of sample used. This ensures that the signal is stable and minimizes the chances of burning the sample. Any fluctuations would indicate that the sample is undergoing changes due to the laser. **Figure 14** compares what the average spectrum of MBA looks like using a 633 nm laser at high (261.57

kW/cm^2) and low (5.85 kW/cm^2) powers. The standard deviation is depicted as the shaded region around the spectra. As previously mentioned, at high laser powers, MBA exhibits spectral fluctuations potentially from photoproducts.[9] Zoltowski et al. observed these fluctuations when 9.38 kW/cm^2 was used, while at lower laser powers only intensity fluctuations were present.[9] Due to the nature of this experiment, it is imperative that the laser has minimal effects on the spectrum to ensure that any effects are attributed to heating by absorption.

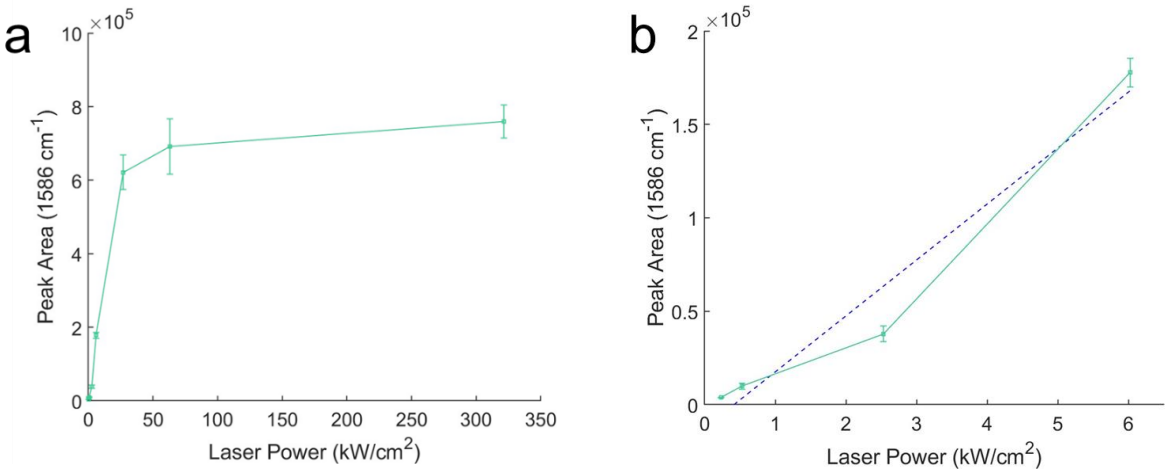

Figure 15. The full curve of the power study for dried MBA functionalized gold nanoparticles (a) using the 633 nm laser. A zoomed in image of the lower linear region with a trendline (b).

To find the optimal laser power, ten 10-second acquisitions were taken at three different spots on the sample at each power setting. Then a fundamental peak of the analyte, MBA (1586 cm^{-1}), was fit in MATLAB to create a plot displaying the relationship between peak area and laser power. For MBA functionalized gold nanoparticles dried onto a glass slide, **Figure 15a** resembles

a Langmuir curve, which is expected since the signal starts to level off at high powers before the sample begins to degrade. Any of the intensities in the lower linear region (**Figure 15b**) are suitable, so the highest power in this region was chosen for analysis (6.02 kW/cm^2). This analysis was also conducted for MBA functionalized gold nanoparticles in solution (396.87 kW/cm^2) as well as silver nanoparticles encapsulated in PAN fibers (74.97 kW/cm^2) on the Renishaw inVia using the 633 nm laser. On the custom microscope, the optimal power using the 785 nm laser for dry nanoparticles was 1.19 kW/cm^2.

3.2 Heating Via Absorption

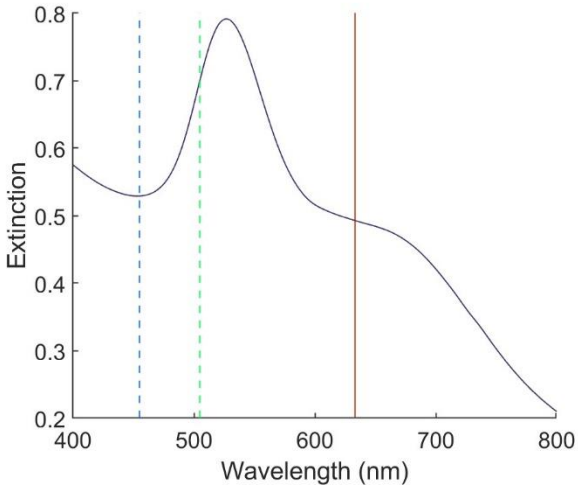

Figure 16. The extinction spectrum of MBA functionalized gold nanoparticles with the 455 and 505 nm LEDs indicated by a dashed line while the 633 nm laser line is denoted by a solid line.

455 and 505 nm LEDs were employed due to their proximity to the plasmon peak. Since the plasmon peak indicates the maximum scattering and absorption, it is necessary to be near it to heat via absorption. The extinction spectrum of the MBA functionalized gold nanoparticles along with the LED powers are shown in **Figure 16**. The LEDs are indicated by the dashed lines while the laser line is shown as a solid line. The dry (**Figure 17a**) and aqueous (**Figure 17b**) samples

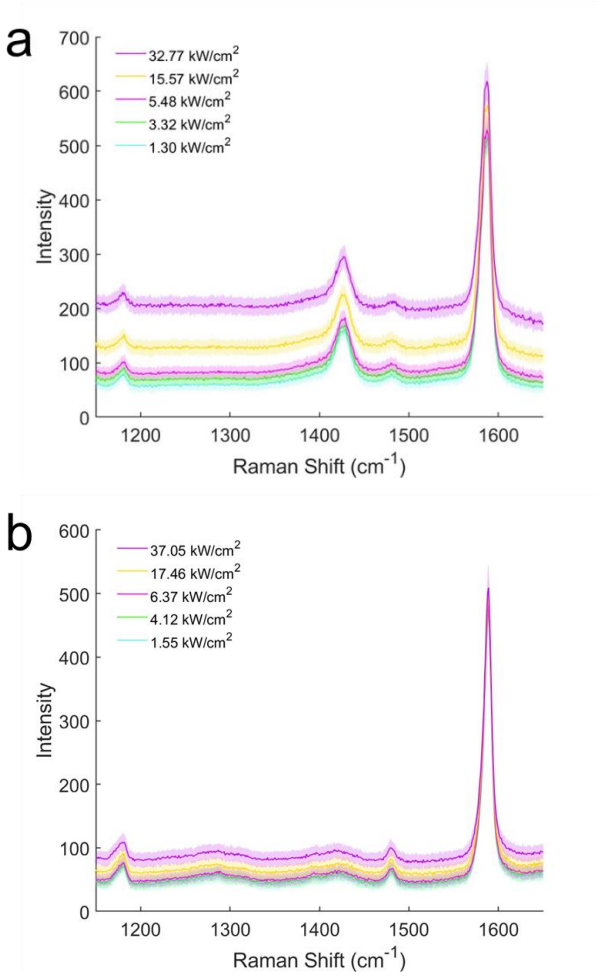

Figure 17. The average signal for increasing 455 nm LED powers for dry (a) and aqueous (b) MBA functionalized gold nanoparticle samples using the 633 nm laser. The standard deviations are the shaded regions.

were analyzed using a 455 nm LED at the optimal laser powers. In **Figure 17**, the average spectrum is shown for each sample at increasing LED power. Prior work has shown that, compared to dry samples, aqueous samples are less affected by increasing power.[34] This is expected as water has a high thermal conductivity enabling it to dissipate heat quickly. It is important to state that for each LED experiment, the 1586 cm^{-1} peak was fit to determine the peak areas before and after the LED acquisitions. The percent difference of these two scans should be less than 10%, which is true for all data shown unless stated otherwise. A percent difference of 10% is an arbitrary threshold based off the typical deviation during each scan. This was determined by taking the average peak area of each spectrum, which was 100 acquisitions, for every experiment that had a percent difference under 10%. The standard deviation and relative standard deviation (RSD) were calculated. Then the overall average RSD and standard deviation were determined to be 5.41% ± 3.39%. Deviations that are much greater than 10%, like 20%, indicate that the sample was becoming damaged or was moving out of focus. During this experiment it is imperative that any changes from the sample are caused by the LED. It is expected that the 1580 cm^{-1} peak does not undergo significant changes due to heating as it originates from the aromatic ring. However, the peak area could deviate due to heating from the LED, which remains a possibility. Data sets that are significantly above the 10% threshold are assumed to be damaged or caused by a complication during the experiment, which is discussed later on.

A 505 nm LED was also used to analyze these samples (**Figure 18**), which yielded graphs similar to those in **Figure 17**. The power density for the dry sample illuminated by the 505 nm LED (**Figure 18a)** is roughly two times more powerful than the 455 nm LED (**Figure 17a**), which

partially explains the larger background increases when using the 505 nm LED. The aqueous sample exhibited larger background increases with the 505 nm (**Figure 18b**) than the 455 nm

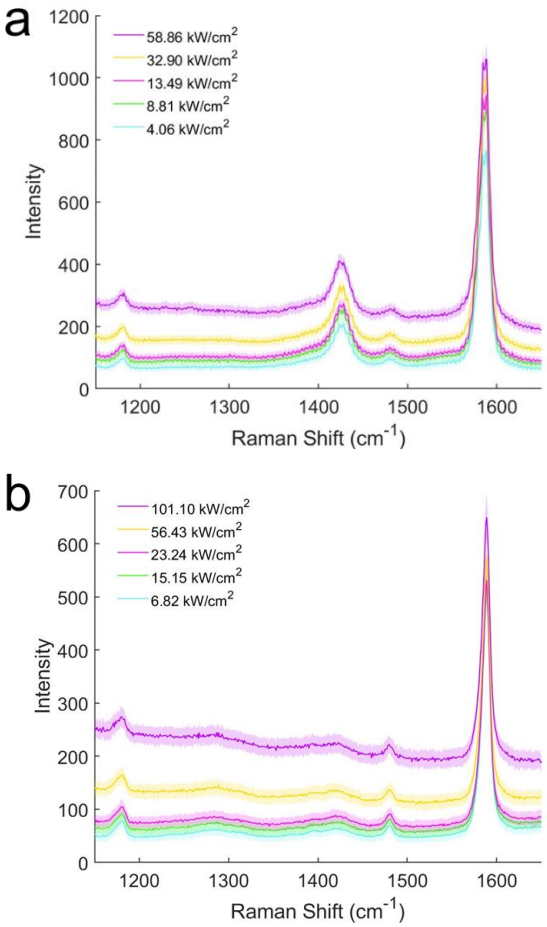

Figure 18. The average signal for increasing 505 nm LED powers for dry (a) and aqueous (b) MBA functionalized gold nanoparticle samples using the 633 nm laser. The standard deviations are the shaded regions.

(**Figure 17b**), which was likely due to the increased power density. Unfortunately, using either LED, even at their highest powers, did not induce any spectral fluctuations. However, the background was observed to increase linearly with LED power, which will be discussed more later.

The percent difference of **Figure 18a** is 11.90%, which is above the threshold. Unfortunately, the dry analyses with the 505 nm LED did not fall below 10% due to refocusing issues. During the first several months of this investigation, the focus was readjusted between scans, which involved moving the microscope shutter two times between acquisitions. This was to ensure that the focus was optimal during the whole analysis because the Raman intensity will decrease if the sample becomes unfocused. However, it will also decrease if the focus is not consistent. Refocusing with the LED on was very difficult and likely caused inconsistent focusing due to cone fatigue, which makes images blurry. Larger deviations in peak area could also stem from replacing the white light source with the respective LED, which ultimately alters the focus due to vibrations. 11.90% is the lowest difference achieved for the 505 nm at suboptimal conditions. This experiment was redone recently, however, the Renishaw inVia was misaligned. Fortunately, more acquisitions can be collected with greater care once the instrument is realigned.

To attempt to see spectral, or frequency, fluctuations, a higher-powered LED was necessary. A new LED (Cool LED pE-400 max) was purchased, equipped with four LED channels: 400, 450, 550, and 635 nm, which are managed by a controller. The channels can be used in tandem as combinations ranging from 0-100% for each LED and the LED can be turned off as the levels are adjusted, which was very convenient for this experiment. 450 nm was utilized as the heating source due to its proximity to previously used LEDs. Combining the 450 and 550 nm channels allowed for a semi-white light source, which simplified the experiment and prevented major stage drift. As briefly mentioned, the white light source had to be mounted on the microscope first. After focusing on to the sample, the white light would be replaced by the LED, as shown in **Figure 19a**, which is held by a screw. The movement from removing the light source would frequently cause the stage to drift, likely in the z direction, causing the sample to move out of focus. Now, the

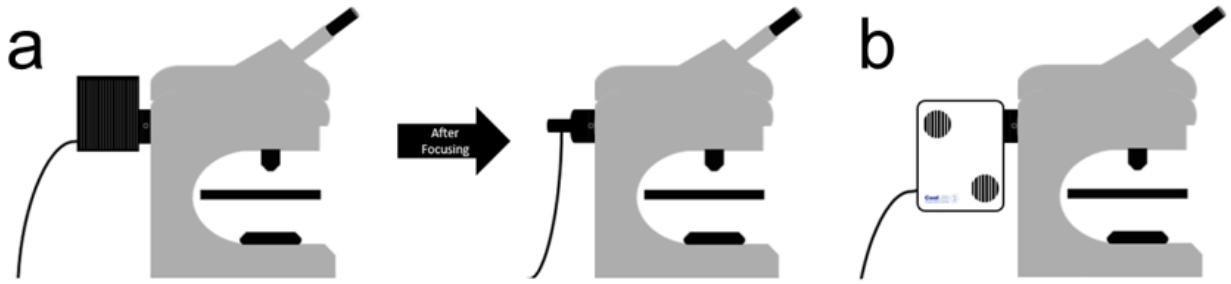

Figure 19. Schematic of the old LED replacing the white light (a) and the new LED that does not need to be removed (b).

multichannel LED remains on the microscope (**Figure 19b**), keeping the focus as consistent as possible. On the Renishaw, a shutter was moved once to open the optical channel to allow the LED to illuminate the sample in tandem with the laser, then once again to close the channel. This was the same shutter that was moved twice between acquisitions in order to readjust the focus between acquisitions. On the custom microscope, the shutter remained open for the complete sequence of analysis while the LED is turned on and off, which removed most of the movement complications. The remaining movement was from closing the laser channel to focus, then reopening it to run the acquisition.

3.3 The Background Trend

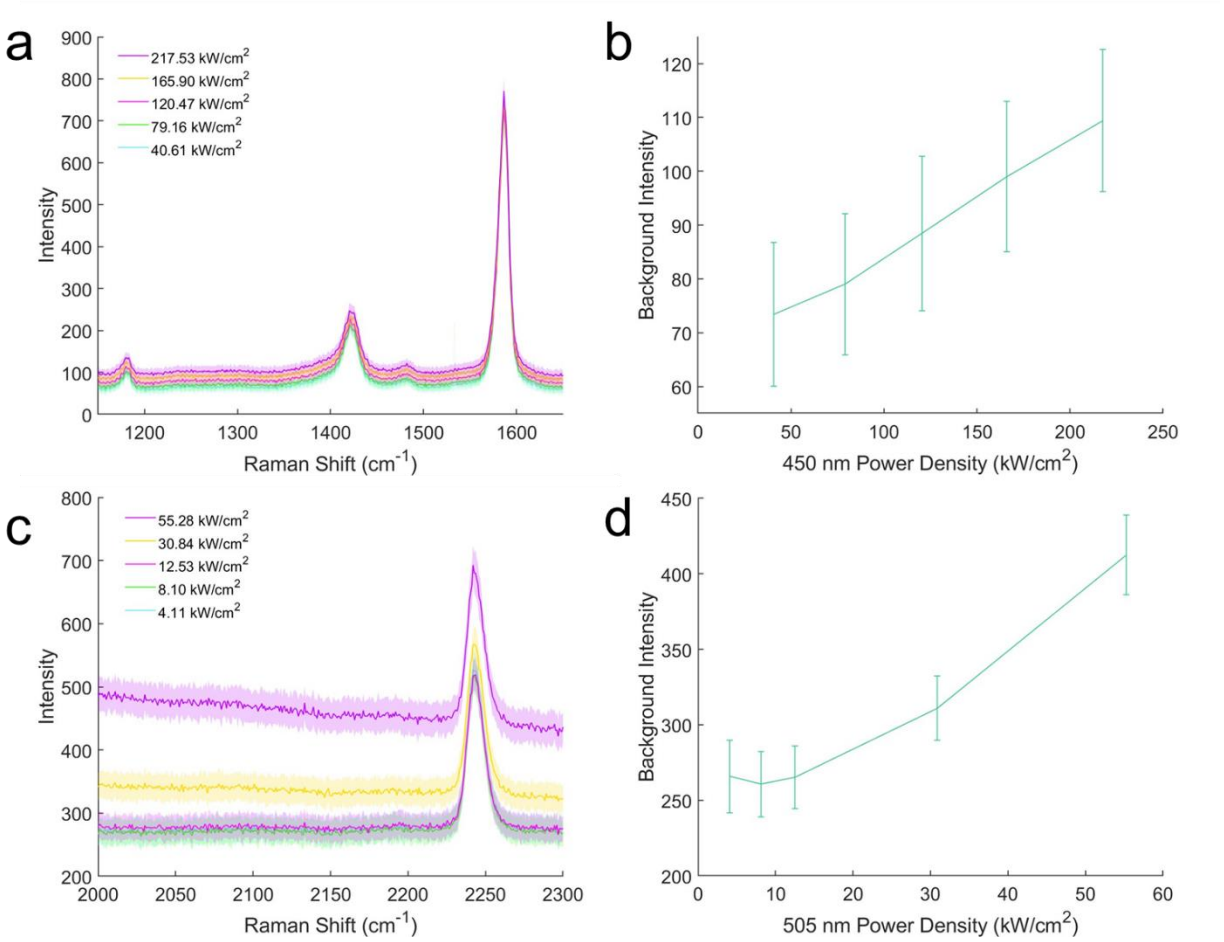

Figure 20. The average signal for increasing 450 nm LED powers for dried MBA functionalized gold nanoparticles (a) with a plot of the background intensity at the respective power density (b). Then the average signal for increasing 505 nm LED powers for silver nanoparticles encapsulated in PAN fibers (c) with a plot of the background intensity at the respective power density (d). Both utilized the 633 nm laser. The standard deviations are the shaded regions.

Using the 450 nm LED with the 633 nm laser did not induce any spectral fluctuations. However, an interesting background effect was observed, which was also present in previous data sets. In **Figure 20a**, the background trend is seen using MBA functionalized gold nanoparticles

with a 450 nm LED. This is clear when looking at **Figure 20b**. The background is averaged at eleven points past the 1586 cm^{-1} peak and the standard deviation is calculated for the error bars. **Figure 20c** shows the same trend but with silver nanoparticles encapsulated in PAN fibers using a 505 nm LED in tandem with the 633 nm laser. The peak that was survielled is a nitrile peak at 2242 cm^{-1}. This peak is suspected to shift when it is in an electric field. However, the peak fitted centers did not seem to have any correlation to the LED power. In **20d**, the trend does not begin significantly increasing until 12.53 kW/cm^2 is reached. This background dependence on LED power persists to a different kind of sample, which is interesting. When revisiting older data, this background effect was present as seen in **Figure 17** and **18**.

On the custom microscope, a 785 nm laser was used, which prevented the 450 nm from being used due to the second order of the LED overriding any signal to be had. So, the 550 nm and 635 nm LEDs were used instead. In **Figure 21**, the LED sequences from the lowest to highest power then back to the lowest power to ensure that the experiment is reversible. In both cases, with the 550 nm (**21a**) and the 635 nm (**21c**), the reverse sequence lines up nicely to the forward sequence while maintaining a threshold below 4%. No fluctuations were observed, but the background trend using the 550 nm and the 635 nm are shown in **Figure 21b** and **21d**, respectively along with the peak area of the 1586 cm^{-1} peak. The forward sequence is depicted as the lighter shade of green and blue, while the reverse sequence is darker. Despite the same trend being observed using both LEDs, the background emissions do not look as similar to each other as the 505 nm, 455 nm, 450 nm do, which will be discussed later on.

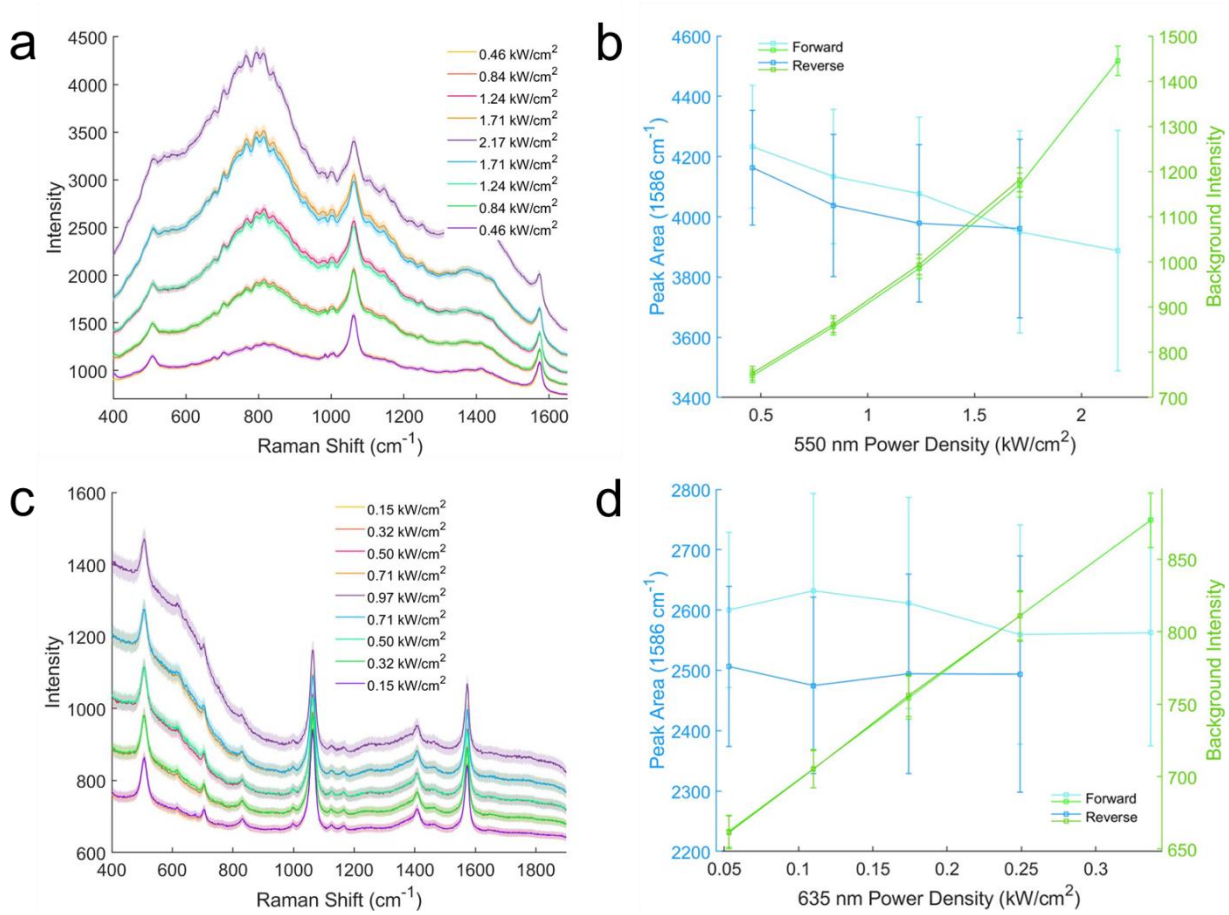

Figure 21. The average signal for increasing 550 nm (a) and 635 nm (c) LED powers for dried MBA functionalized gold nanoparticles using the 785 nm laser. The standard deviations are the shaded regions. b and d are plots exhibiting the peak area of the 1586 cm-1 peak along with the respective background intensity at each power are shown. The forward and reverse sequence are shown for both.

In the past, increases in the background were observed with increasing laser power.[6,8] In **Figure 22a**, the background is seen to increase linearly with the power of a 532 nm laser.[6] They theorized that this was due to gold's interaction with graphitic carbon on the surface of the gold leading to a promotion of chemical interface dampening and a reduced plasmon dephasing time. During the laser power studies, the background increased steadily with laser power even at the

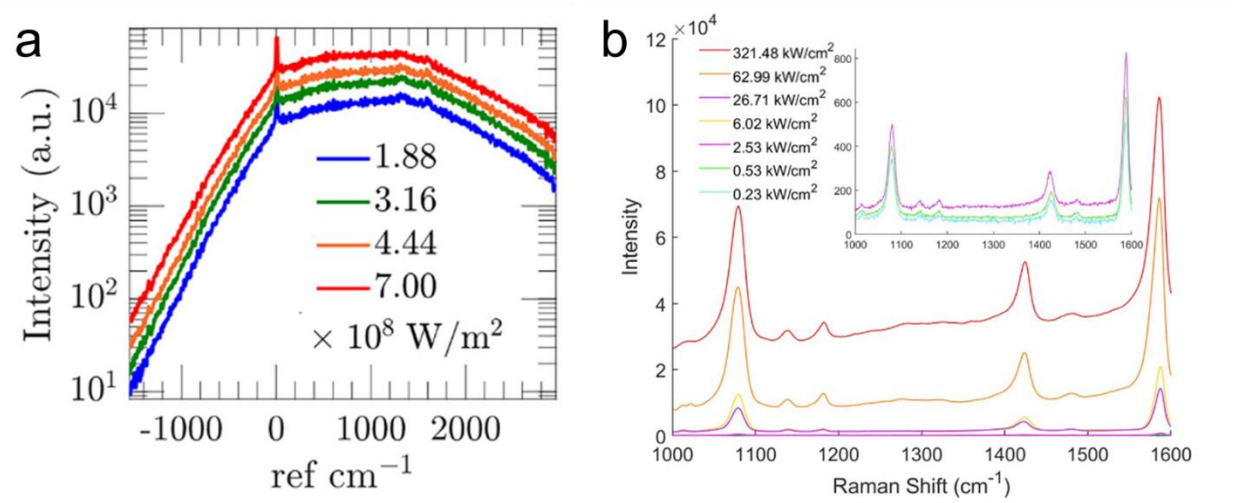

Figure 22. The background increasing due to increasing laser power on gold nanodisks (a).[6] The spectrum of increasing laser power densities for dried MBA functionalized gold nanoparticles using the 633 nm laser (b). The inset is of the three lowest densities.

lowest power densities as shown in **Figure 22b**. However, since a reasonable laser power density was utilized, this increase is likely from electron transfers that are dependent on the LED wavelength and power. Hugall et al. observed background increases due to the temperature reaching over 360 K. They theorized this was due to molecular desorption roughening the gold surface.[4] This is unlikely in the context of this experiment because this trend has proven to be reversible and the threshold ensures that there is minimal damage to the surface.

Mahajan et al. also saw the background increase but due to molecular exchange.[5] They replaced p-nitrobenzenethiol (NBT) with p-methoxybenzenethiol, or an electron withdrawing group with a more electron donating group. When it was replaced they noticed a decrease in background intensity. So, they did it again using NBT and MBA as a less electron withdrawing group. When MBA replaced NBT the background decreased again. To ensure it is a trend they also replaced MBA with NBT and saw the background increase. They hypothesized that electron

withdrawing molecules pull electrons from the metal to the surface, which increased the internal electric field as well as the background emission.[5]

While this could be possible, from the experiments conducted it is hypothesized that this background increase has major contributions from electron transfers mediated by the LSPR. This is supported by the differently shaped background emissions from the various LEDs. Jain et al. studied the wavelength dependence on gold nanorods that are acting as a plasmonic photocatalyst to regenerate NADH cofactors.[40] They used gold nanorods functionalized with negatively charged 11-Mercaptoundecanoic acid along with triethanolamine as the hole scavenger and $[Cp^*Rh(bpy)(H2O)]^{2+}$ as the electron mediator. Their excitation wavelengths were 450, 532, and 808 nm to investigate gold's wavelength dependence on its threshold energy for interband transitions (~2.1 eV). They observed the highest photoregeneration from the 450 nm while 808 nm had the lowest due to 450 nm being above the threshold. It was theorized that this was due to higher energy hot carriers with a longer lifetime.[40] When comparing their results to those presented, it would make sense that the background emission observed is dependent on the LED wavelength. **Figure 23** displays the LSPR with the LED wavelengths indicated by dashed lines and the respective laser wavelength used as a solid line. In **Figure 23a**, the LEDs used in tandem with the 633 nm laser are shown and all of the LED wavelengths are above the threshold energy. **Figure 23c** displays the 785 nm laser along with the two LEDs used, which only 550 is above the threshold energy. **Figure 23b** and **d** present this trend and the wavelengths that are closest to the plasmon peak seem to have the greatest influence on the background. For simplicity, only the forward LED sequence is shown for the 550 and 635 nm in **Figure 23d**.

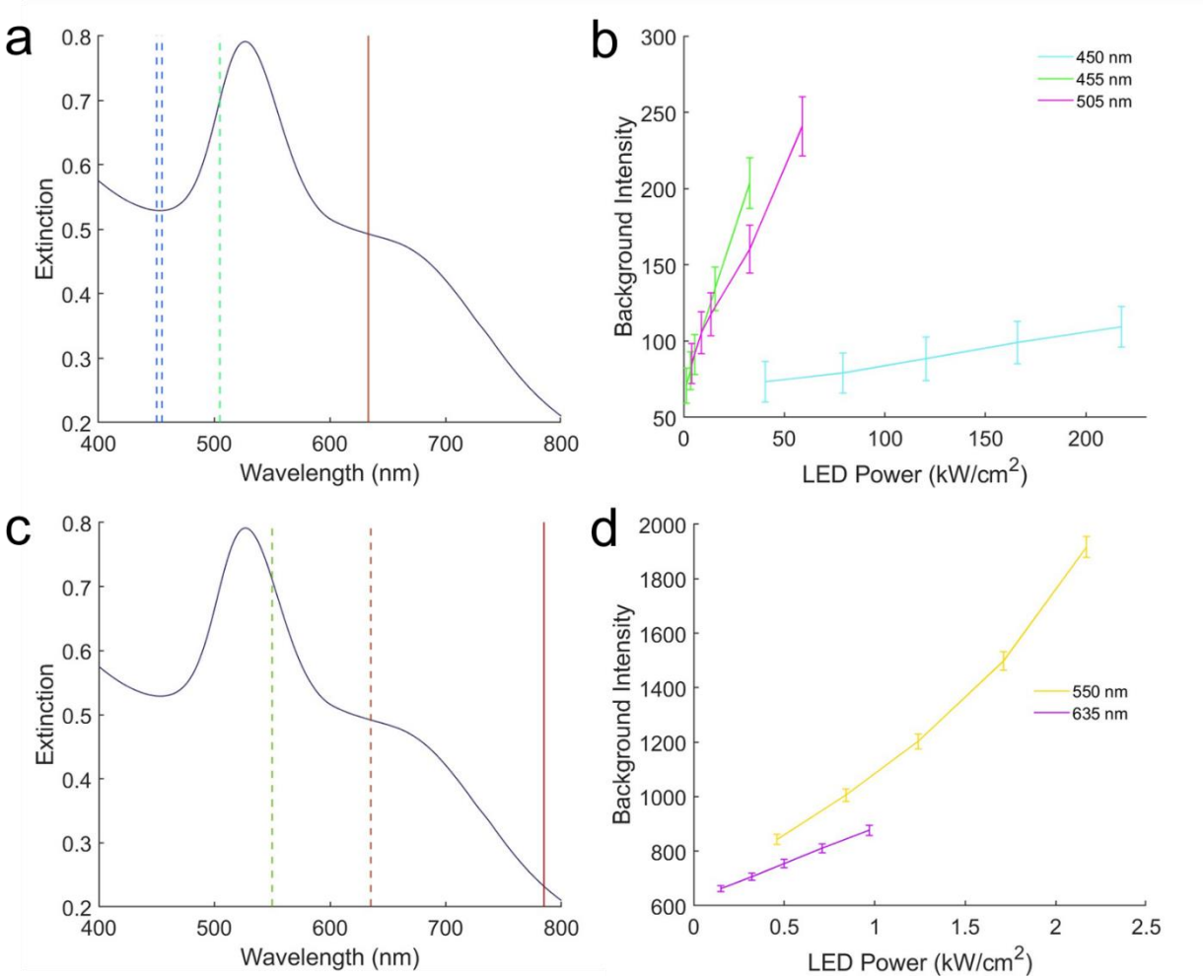

Figure 23. The LSPR of the MBA functionalized nanoparticles with dashed lines indicating an LED while the solid lines indicate the laser wavelength for 633 nm (a) and 785 nm (c). b and d display the background intensity at each LED power for each LED used with the respective laser. For d, only the forward sequence is shown for each LED.

When comparing **Figures 17a, 18a, and 20a** the background emission shape looks very similar. However, when the 450 nm was used the background did not increase nearly as much as the 455 and 505 nm despite having significantly more power. This descrepency could be caused by the lack of refocusing between acquisitions. As previously mentioned, refcusing with the LED

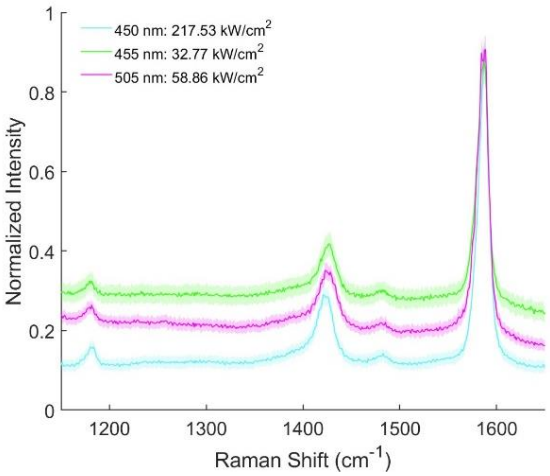

Figure 24. The average spectrum of the highest LED power for each LED used with the 633 nm laser. Normalized to the most intense point during the acquisitions. The standard deviations are the shaded regions.

on can cause cone fatigue, which would cause inconsistent focusing. However, it is more probable that a greater contribution stems from the proximity to the plasmon peak. The 505 nm was the closest out of the three there seems to be a slight increase in background starting around 1300 cm^{-1}. In **Figure 24**, the highest LED power for each wavelength was normalized to the most intense signal in their respective data set. It is peculiar as to why the background for the 450 nm is lower than the 455 nm, especially since it had a larger power density. However, it is possible that this decrease is caused by inconsistent focusing as well. The slope is apparent for the 505 nm and is theorized to come from higher energy electrons contributing to the background. The 505 nm lies on the plasmon peak, which increases the absorption as well as the scattering. It is plausable that as the plasmon decays, charge transfer occurs as those electrons relax via photoluminescence. Since the 450 and 455 nm are slightly off resonant, they do not experience the same effects.

When looking at **Figure 21**, it is clear that there are distinct differences in the background contiuum. The 550 nm is 1 nm closer to the plasmon peak than the 505 nm, but both are above the threshold energy for interband transitions. While the 1 nm difference may end up being insignificant, the placement on the LSPR could be important. The 505 nm is to the blue of the peak while the 550 nm is to the red but the signifance of this is not understood. It is likely that charge transfer is also occuring when using 550 nm excitation, however the cause of major increase in the background is not clear. So, it is hypothesized that being to the red or blue of the plasmon maximum has a major contribution to the background emission. Meanwhile, the 635 nm is further from the maximum plasmon peak, lying on the shoulder which is likely due to aggregation. This energy is below the transition energy, but still experiences an abnormal background increase around 1000 cm^{-1}, which could be due to the proximity of the aggregation plasmon. This energy could be facilitating intraband transitions instead, contributing to the significant increase in the higher energy region of the Stokes spectrum. So, it is likely that the proximity of the absorption wavelength to either plasmon peak has major effects on the background emission. These are just theories as the mechanism that is responsible for this phenomena is highly complex and difficult to probe. However, in the future more experiments can be done to attempt to elucidate this trend further.

Chapter 4: Conclusion

This thesis investigated the wavelength dependence of the background emission evident in the Raman spectra from MBA functionalized gold nanoparticles with co-illuminating LEDs. The shape of the background seems to change majorly when the absorption is to the red of the plasmon peak (550 nm), causing uneven baselines. When it is to the blue (505 nm), the emission is flatter in comparison, however, there is a slight negative slope near 1200 cm^{-1}. If a 450 or 455 nm LED is used, the backgrounds look similar and do not seem to have any abnormal increases. Neither LED are resonant with the plasmon maximum, so they do not experience the same effects. When a 635 nm LED is used, the background increases in general, but more significantly on the higher end of the Stokes region. This energy is resonant on the plasmon peak that is assumed to be due to aggregates, so the background could have contributions from this plasmon. The major background increase could be due to intraband transitions, contributing to the increasing background. Since the energy of a 505 and 550 nm are both resonant on the single nanoparticle plasmon peak, it is hypothesized that they absorb the energy and as the LSPR decays, charge transfer occurs as those electrons relax by photoluminescence. However, the extreme background observed when using the 550 nm LED is not well understood, so it is hypothesized that being to the red or blue of the plasmon maximum has a major contribution. The exact mechanism is unknown, and it is difficult to probe. So, more experiments will to be conducted to attempt to elucidate this trend further.

In the future, the same experiment will be conducted on bare gold nanoparticles to see if the same effect is observed. Then the 505 and 455 nm will be used in tandem with a 785 nm to compare the spectrums using a 633 nm laser. It would also be beneficial to use a 633 nm on the custom microscope to measure the anti-Stokes region to extract the temperature and compare to

other research papers. Lastly, it would be interesting to use mercaptobenzonitrile, which has peaks known to shift in the presence of electric fields. This would be valuable to determine if this background trend is observed over various samples.

Bibliography

(1) Chen, D.; Zhu, X.; Huang, J.; Wang, G.; Zhao, Y.; Chen, F.; Wei, J.; Song, Z.; Zhao, Y. Polydopamine@Gold Nanowaxberry Enabling Improved SERS Sensing of Pesticides, Pollutants, and Explosives in Complex Samples. *Anal. Chem.* **2018**, *90* (15), 9048–9054. https://doi.org/10.1021/acs.analchem.8b01348.

(2) Bhardwaj, K.; Jaiswal, A. Plasmonic 3-D Wrinkled Polymeric Shrink Film-Based SERS Substrates for Pesticide Detection on Real-World Surfaces. *Analyst* **2023**, *148* (3), 562–572. https://doi.org/10.1039/D2AN01657E.

(3) Wang, H.; Xue, Z.; Wu, Y.; Gilmore, J.; Wang, L.; Fabris, L. Rapid SERS Quantification of Trace Fentanyl Laced in Recreational Drugs with a Portable Raman Module. *Anal. Chem.* **2021**, *93* (27), 9373–9382. https://doi.org/10.1021/acs.analchem.1c00792.

(4) Hugall, J. T.; Baumberg, J. J. Demonstrating Photoluminescence from Au Is Electronic Inelastic Light Scattering of a Plasmonic Metal: The Origin of SERS Backgrounds. *Nano Lett.* **2015**, *15* (4), 2600–2604. https://doi.org/10.1021/acs.nanolett.5b00146.

(5) Mahajan, S.; Cole, R. M.; Speed, J. D.; Pelfrey, S. H.; Russell, A. E.; Bartlett, P. N.; Barnett, S. M.; Baumberg, J. J. Understanding the Surface-Enhanced Raman Spectroscopy "Background." *J. Phys. Chem. C* **2010**, *114* (16), 7242–7250. https://doi.org/10.1021/jp907197b.

(6) Wu, S.; Cheng, O. H.-C.; Zhao, B.; Hogan, N.; Lee, A.; Son, D. H.; Sheldon, M. The Connection between Plasmon Decay Dynamics and the Surface Enhanced Raman Spectroscopy Background: Inelastic Scattering from Non-Thermal and Hot Carriers. *Journal of Applied Physics* **2021**, *129* (17), 173103. https://doi.org/10.1063/5.0032763.

(7) Sun, S.; Rathnayake, D. T.; Guo, Y. Asymmetrical Spectral Continuum between Anti-Stokes and Stokes Scattering Revealed in Low-Frequency Surface-Enhanced Raman Spectroscopy. *The Journal of Physical Chemistry C* **2022**, *126* (27). https://doi.org/10.1021/acs.jpcc.2c02486.

(8) Zhu, Y.; Natelson, D.; Cui, L. Probing Energy Dissipation in Molecular-Scale Junctions via Surface Enhanced Raman Spectroscopy: Vibrational Pumping and Hot Carrier Enhanced Light Emission. *J. Phys.: Condens. Matter* **2021**, *33* (13), 134001. https://doi.org/10.1088/1361-648X/abda7b.

(9) Zoltowski, C. M.; Shoup, D. N.; Schultz, Z. D. Investigation of SERS Frequency Fluctuations Relevant to Sensing and Catalysis. *J. Phys. Chem. C* **2022**, *126* (34), 14547–14557. https://doi.org/10.1021/acs.jpcc.2c03150.

(10) Wang, P.; Li, X.; Sun, Y.; Wang, L.; Xu, Y.; Li, G. Rapid and Reliable Detection and Quantification of Organophosphorus Pesticides Using SERS Combined with Dispersive Liquid–Liquid Microextraction. *Anal. Methods* **2022**, *14* (45), 4680–4689. https://doi.org/10.1039/D2AY01321E.

(11) Sarfo, D. K.; Sivanesan, A.; Izake, E. L.; Ayoko, G. A. Rapid Detection of Mercury Contamination in Water by Surface Enhanced Raman Spectroscopy. *RSC Adv.* **2017**, *7* (35), 21567–21575. https://doi.org/10.1039/C7RA02209C.

(12) Guven, B.; Eryilmaz, M.; Üzer, A.; Boyaci, I. H.; Tamer, U.; Apak, R. Surface-Enhanced Raman Spectroscopy Combined with Gold Nanorods for the Simultaneous Quantification of Nitramine Energetic Materials. *RSC Adv.* **2017**, *7* (59), 37039–37047. https://doi.org/10.1039/C7RA05844F.

(13) *Modern Raman Spectroscopy*, 1st ed.; John Wiley & Sons, Ltd, 2019. https://doi.org/10.1002/9781119440598.
(14) Zani, V.; Pedron, D.; Pilot, R.; Signorini, R. Contactless Temperature Sensing at the Microscale Based on Titanium Dioxide Raman Thermometry. *Biosensors (Basel)* **2021**, *11* (4), 102. https://doi.org/10.3390/bios11040102.
(15) Stiles, P. L.; Dieringer, J. A.; Shah, N. C.; Van Duyne, R. P. Surface-Enhanced Raman Spectroscopy. *Annual Review of Analytical Chemistry* **2008**, *1* (1), 601–626. https://doi.org/10.1146/annurev.anchem.1.031207.112814.
(16) Willets, K. A.; Van Duyne, R. P. Localized Surface Plasmon Resonance Spectroscopy and Sensing. *Annu. Rev. Phys. Chem.* **2007**, *58* (1), 267–297. https://doi.org/10.1146/annurev.physchem.58.032806.104607.
(17) Dvoynenko, M. M.; Wang, H.-H.; Hsiao, H.-H.; Wang, Y.-L.; Wang, J.-K. Study of Signal-to-Background Ratio of Surface-Enhanced Raman Scattering: Dependences on Excitation Wavelength and Hot-Spot Gap. *J. Phys. Chem. C* **2017**, *121* (47), 26438–26445. https://doi.org/10.1021/acs.jpcc.7b08362.
(18) Debnath, D.; Ghosh, S. K. Optical Constants of Noble Metals at the Nanoscale within the Framework of the Drude Free-Electron Conduction Model: Implications for Liquid Crystal Sensing. *ACS Appl. Nano Mater.* **2022**, *5* (1), 1621–1634. https://doi.org/10.1021/acsanm.1c04393.
(19) Wiley, B. J.; Chen, Y.; McLellan, J. M.; Xiong, Y.; Li, Z.-Y.; Ginger, D.; Xia, Y. Synthesis and Optical Properties of Silver Nanobars and Nanorice. *Nano Lett.* **2007**, *7* (4), 1032–1036. https://doi.org/10.1021/nl070214f.
(20) McFarland, A. D.; Van Duyne, R. P. Single Silver Nanoparticles as Real-Time Optical Sensors with Zeptomole Sensitivity. *Nano Lett.* **2003**, *3* (8), 1057–1062. https://doi.org/10.1021/nl034372s.
(21) Farooq, S.; de Araujo, R. Engineering a Localized Surface Plasmon Resonance Platform for Molecular Biosensing. *Open Journal of Applied Sciences* **2018**, *08*, 126–139. https://doi.org/10.4236/ojapps.2018.83010.
(22) Zhao, J.; Das, A.; Zhang, X.; Schatz, G. C.; Sligar, S. G.; Van Duyne, R. P. Resonance Surface Plasmon Spectroscopy: Low Molecular Weight Substrate Binding to Cytochrome P450. *J. Am. Chem. Soc.* **2006**, *128* (34), 11004–11005. https://doi.org/10.1021/ja0636082.
(23) Muravitskaya, A.; Movsesyan, A.; Ávalos-Ovando, O.; Bahamondes Lorca, V. A.; Correa-Duarte, M. A.; Besteiro, L. V.; Liedl, T.; Yu, P.; Wang, Z.; Markovich, G.; Govorov, A. O. Hot Electrons and Electromagnetic Effects in the Broadband Au, Ag, and Ag–Au Nanocrystals: The UV, Visible, and NIR Plasmons. *ACS Photonics* **2024**, *11* (1), 68–84. https://doi.org/10.1021/acsphotonics.3c00951.
(24) Petryayeva, E.; Krull, U. J. Localized Surface Plasmon Resonance: Nanostructures, Bioassays and Biosensing—A Review. *Analytica Chimica Acta* **2011**, *706* (1), 8–24. https://doi.org/10.1016/j.aca.2011.08.020.
(25) Chatterjee, S.; Ringane, A. B.; Arya, A.; Das, G. M.; Dantham, V. R.; Laha, R.; Hussian, S. A High-Yield, One-Step Synthesis of Surfactant-Free Gold Nanostars and Numerical Study for Single-Molecule SERS Application. *J Nanopart Res* **2016**, *18* (8), 242. https://doi.org/10.1007/s11051-016-3557-0.
(26) Höller, R. P. M.; Kuttner, C.; Mayer, M.; Wang, R.; Dulle, M.; Contreras-Cáceres, R.; Fery, A.; Liz-Marzán, L. M. Colloidal Superstructures with Triangular Cores: Size Effects on SERS

Efficiency. *ACS Photonics* **2020**, *7* (7), 1839–1848. https://doi.org/10.1021/acsphotonics.0c00642.
(27) Zhao, Q.; Hilal, H.; Kim, J.; Park, W.; Haddadnezhad, M.; Lee, J.; Park, W.; Lee, J.-W.; Lee, S.; Jung, I.; Park, S. All-Hot-Spot Bulk Surface-Enhanced Raman Scattering (SERS) Substrates: Attomolar Detection of Adsorbates with Designer Plasmonic Nanoparticles. *J. Am. Chem. Soc.* **2022**, *144* (29), 13285–13293. https://doi.org/10.1021/jacs.2c04514.
(28) Zhang, Y.; Gu, Y.; He, J.; Thackray, B. D.; Ye, J. Ultrabright Gap-Enhanced Raman Tags for High-Speed Bioimaging. *Nat Commun* **2019**, *10* (1), 3905. https://doi.org/10.1038/s41467-019-11829-y.
(29) Zhu, W.; Crozier, K. B. Quantum Mechanical Limit to Plasmonic Enhancement as Observed by Surface-Enhanced Raman Scattering. *Nat Commun* **2014**, *5* (1), 5228. https://doi.org/10.1038/ncomms6228.
(30) Dieringer, J. A.; McFarland, A. D.; Shah, N. C.; Stuart, D. A.; Whitney, A. V.; Yonzon, C. R.; Young, M. A.; Zhang, X.; Duyne, R. P. V. Surface Enhanced Raman Spectroscopy: Newmaterials, Concepts, Characterization Tools, and Applications. *Faraday Discuss.* **2006**, *132* (0), 9–26. https://doi.org/10.1039/B513431P.
(31) Linic, S.; Aslam, U.; Boerigter, C.; Morabito, M. Photochemical Transformations on Plasmonic Metal Nanoparticles. *Nature Mater* **2015**, *14* (6), 567–576. https://doi.org/10.1038/nmat4281.
(32) Nehra, K.; Pandian, S. K.; Byram, C.; Moram, S. S. B.; Soma, V. R. Quantitative Analysis of Catalysis and SERS Performance in Hollow and Star-Shaped Au Nanostructures. *J. Phys. Chem. C* **2019**, *123* (26), 16210–16222. https://doi.org/10.1021/acs.jpcc.9b03086.
(33) Hong, S.; Li, X. Optimal Size of Gold Nanoparticles for Surface-Enhanced Raman Spectroscopy under Different Conditions. *Journal of Nanomaterials* **2013**, *2013*, e790323. https://doi.org/10.1155/2013/790323.
(34) Zeng, Z.-C.; Wang, H.; Johns, P.; Hartland, G. V.; Schultz, Z. D. Photothermal Microscopy of Coupled Nanostructures and the Impact of Nanoscale Heating in Surface-Enhanced Raman Spectroscopy. *J. Phys. Chem. C* **2017**, *121* (21), 11623–11631. https://doi.org/10.1021/acs.jpcc.7b01220.
(35) Shin, G.; Lim, D.; Shin, D. Plasmonic Heating Effect in SERS-Based Nanoplastic Detection. *Sensors and Actuators B: Chemical* **2023**, *393*, 134196. https://doi.org/10.1016/j.snb.2023.134196.
(36) Xu, Y.; Wang, Y.; Chen, Y.; Yue, Y.; Jiang, J. Temperature Dependence of Raman Enhancement Induced by Au Nanorods Array. *Mater. Res. Express* **2018**, *5* (6), 065057. https://doi.org/10.1088/2053-1591/aabab9.
(37) Saikin, S. K.; Chu, Y.; Rappoport, D.; Crozier, K. B.; Aspuru-Guzik, A. Separation of Electromagnetic and Chemical Contributions to Surface-Enhanced Raman Spectra on Nanoengineered Plasmonic Substrates. *J. Phys. Chem. Lett.* **2010**, *1* (18), 2740–2746. https://doi.org/10.1021/jz1008714.
(38) Schmidt, M. M.; Farley, E. A.; Engevik, M. A.; Adelsman, T. N.; Tuckmantel Bido, A.; Lemke, N. D.; Brolo, A. G.; Lindquist, N. C. High-Speed Spectral Characterization of Single-Molecule SERS Fluctuations. *ACS Nano* **2023**, *17* (7), 6675–6686. https://doi.org/10.1021/acsnano.2c12457.
(39) Frens, G. Controlled Nucleation for the Regulation of the Particle Size in Monodisperse Gold Suspensions. *Nature Physical Science* **1973**, *241* (105), 20–22. https://doi.org/10.1038/physci241020a0.

(40) Jain, V.; Chakraborty, I. N.; Raj, R. B.; Pillai, P. P. Deciphering the Role of Light Excitation Attributes in Plasmonic Photocatalysis: The Case of Nicotinamide Cofactor Regeneration. *J. Phys. Chem. C* **2023**, *127* (10), 5153–5161. https://doi.org/10.1021/acs.jpcc.2c08678.